Oxygen Activity in Li-Rich Disordered Rock-Salt Oxide and the Influence of $LiNbO_3$ Surface Modification on the Electrochemical Performance

Musa Ali Cambaz,[†] Bhaghavathi P. Vinayan,[†] Holger Geßwein,[‡] Alexander Schiele,[§] Angelina Sarapulova,[‡] Thomas Diemant,[∥] Andrey Mazilkin,[§,⊥] Torsten Brezesinski,[§] R. Jürgen Behm,[†,∥] Helmut Ehrenberg,[†,‡] and Maximilian Fichtner*[,†,§]

[†]Helmholtz Institute Ulm (HIU) Electrochemical Energy Storage, Helmholtzstrasse 11, 89081 Ulm, Germany

[‡]Institute for Applied Materials, Karlsruhe Institute of Technology (KIT), Herrmann von Helmholtz Platz 1, 76344 Eggenstein Leopoldshafen, Germany

[§]Institute of Nanotechnology, Karlsruhe Institute of Technology (KIT), Herrmann von Helmholtz Platz 1, 76344 Eggenstein Leopoldshafen, Germany

[∥]Institute of Surface Chemistry and Catalysis, Ulm University, Albert Einstein Allee 47, 89081 Ulm, Germany

[⊥]Institute of Solid State Physics of the Russian Academy of Sciences, Academician Ossipyan Street 2, 142432 Chernogolovka, Russia

ABSTRACT: Li rich disordered rock salt oxides such as $Li_{1.2}Ni_{1/3}Ti_{1/3}Mo_{2/15}O_2$ are receiving increasing attention as high capacity cathodes due to their potential as high energy materials with variable elemental composition. However, the first cycle oxygen release lowers the cycling performance due to cation densification and structural reconstruction on the surface region. This work explores the influence of lithium excess on the charge compensation mechanism and the effect of surface modification with $LiNbO_3$ on the cycling performance. Moving from a stoichiometric $LiNi_{0.5}Ti_{0.5}O_2$ composition toward Li rich $Li_{1.2}Ni_{1/3}Ti_{1/3}Mo_{2/15}O_2$, oxygen redox is accompanied by oxygen release. Thereby, cationic charge compensation is governed by the $Ni^{2+/3+}$ and $Mo^{3+/6+}$ redox reaction. Contrary to the bulk oxidation state of Mo^{6+} in the charged state, a mixed Mo valence on the surface is found by XPS. Furthermore, it is observed that smaller particle sizes result in higher specific capacities. Tailoring the surface properties of $Li_{1.2}Ni_{1/3}Ti_{1/3}Mo_{2/15}O_2$ with a solid electrolyte layer of $LiNbO_3$ altered the voltage profile, resulting in a higher average discharge voltage as compared to the unmodified material. The results hint at the interdiffusion of cations from the metal oxide surface coating into the electrode material, leading to bulk composition changes (doping) and a segregated Nb rich surface. The main finding of this work is the enhanced cycling stability and lower impedance of the surface modified compound. We argue that surface densification is mitigated by the Nb doping/surface modification.

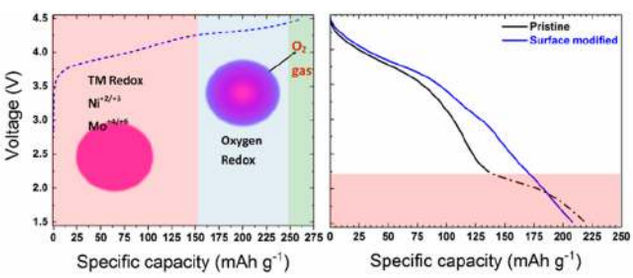

INTRODUCTION

The development of lithium ion batteries (LIBs) with high energy density is one of the primary objectives in the energy storage field. The cathode material is considered as the bottleneck for improving the energy density. Conventional layered oxides like $LiCoO_2$ and $LiNi_{1/3}Mn_{1/3}Co_{1/3}O_2$ exhibit stable specific capacities between 145 and 165 mAh g^{-1}.[1,1−3] Therefore, Li rich layered oxides $xLi_2MnO_3{\cdot}(1-x)LiMO_2$ (M = 3d transition metals), which promise higher capacities, are now pursued as future cathode materials.[4,5] These compounds offer specific capacities exceeding 200 mAh g^{-1}, which results from the fact that charge can be stored on both the transition metal (Tm) cation and the oxygen anion.[6−9] All of these materials have ordered structures. Li rich disordered rock salt oxides (DRS) with α $LiFeO_2$ type structure lately have attracted considerable attention. Even though lithium migration is hindered in cation disordered rock salt oxides, they can in principle function well as high capacity cathode materials. For a threshold ratio lithium:transition metal (Li:Tm) ≥ 1.09, the lithium sites can percolate sufficiently within the structure and form favorable diffusion pathways.[10,11] Recently, Yabuuchi et al.[12,13] demonstrated that for Li rich cation disordered Li_3NbO_4−MO (M = Fe, Ni, Mn), a significant portion of the charge comes from reversible oxygen redox and is not mainly due to oxygen release. Oxygen redox can be beneficial, as it contributes to the capacity in the high voltage range. However,

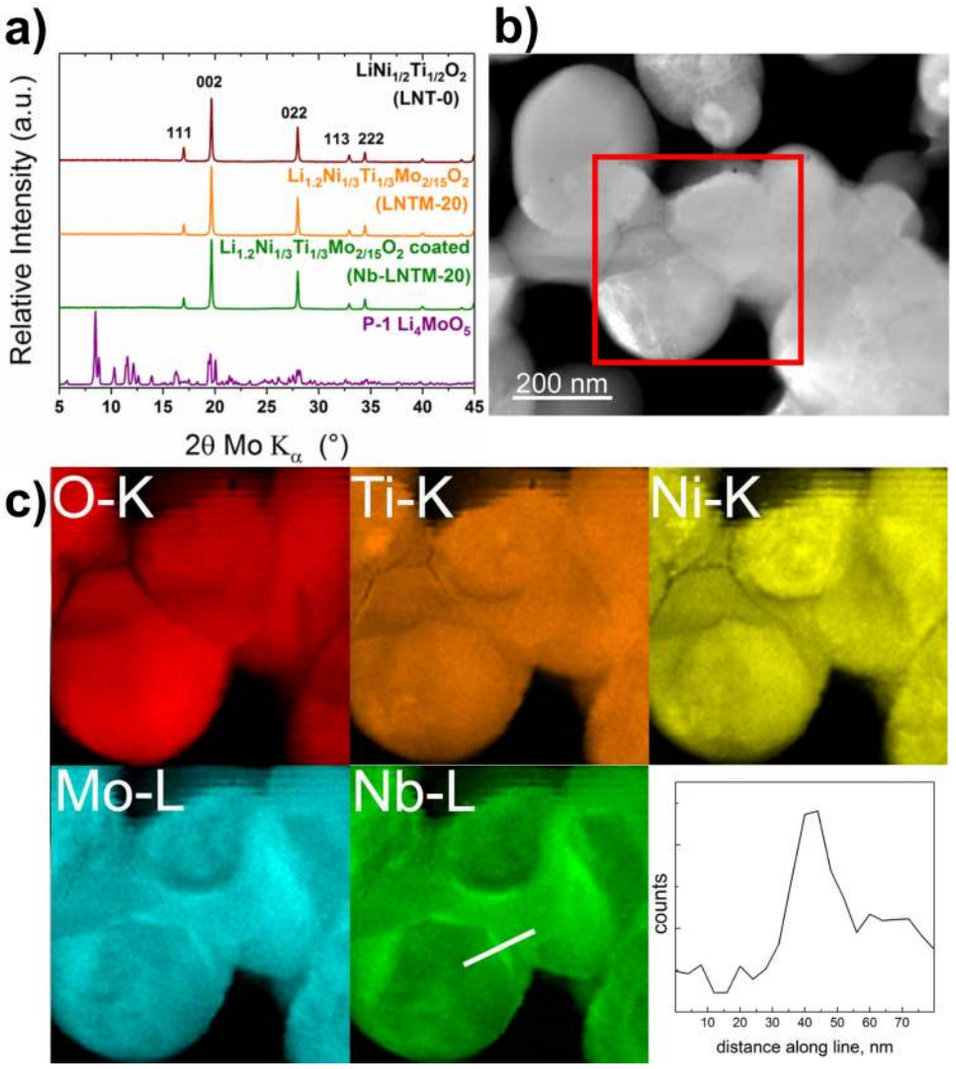

Figure 1. (a) XRD pattern of $LiNi_{1/2}Ti_{1/2}O_2$ (LNT 0), $Li_{1.2}Ni_{1/3}Ti_{1/3}Mo_{2/15}O_2$ (LNTM 20), $LiNbO_3$ coated $Li_{1.2}Ni_{1/3}Ti_{1/3}Mo_{2/15}O_2$ (Nb LNTM 20), and Li_4MoO_5. (b) STEM image of Nb LNTM 20 and (c) EDX mapping results obtained on Nb LNTM 20 and the line profile for the Nb L edge.

too much oxidation seems to be detrimental, as oxygen loss can be triggered. This leads to a near surface cation densification, which can severely impede the Li diffusion.[14] The generation of highly reactive oxygen radicals (in the form of O_2^-/O^- or O_2^{2-} in the bulk of the material) or even oxygen vacancies (after oxygen loss) on the particle surface during the electrochemical process is presumed to result in the formation of a resistive surface layer due to electrolyte decomposition and structural transformation.[15−17] Thus, strategies to stabilize the particle surface to alleviate or even overcome these problems are needed to improve the performance of Li rich disordered rock salt oxides.

$Li_{1.2}Ni_{1/3}Ti_{1/3}Mo_{2/15}O_2$ is a promising cathode material that exhibits high specific capacities but suffers from oxygen release.[10,18] Here, we propose a surface modification strategy using $LiNbO_3$ in order to reduce the surface degradation and improve the electrochemical performance.[19,20]

■ RESULT AND DISCUSSION

Synthesis and Characterization. We chose to investigate a solid solution between the stoichiometric cation disordered *Fm*3*m* Li_2NiTiO_4 ($LiNi_{0.5}Ti_{0.5}O_2$) and the lithium enriched cation ordered *P*1 Li_4MoO_5($Li_{1.6}Mo_{0.4}O_2$), targeting lithium rich cation disordered Li−Ni−Ti−Mo oxide. For a clear representation of the lithium to transition metal ratio, we use the notation $LiMO_2$. $LiNi_{0.5}Ti_{0.5}O_2$ is adopting an α $LiFeO_2$ type crystal structure, where Li and the transition metals share the same octahedral site and are randomly distributed without any long range order. These types of compounds are referred to as cation disordered rock salt oxides in the literature.[21] Depending on the degree of the random occupation (from partial to full occupancy), the extent of cation disorder varies. For the cation ordered triclinic *P*1 Li_4MoO_5, Mo^{6+} ions occupy the octahedral sites in a cubic close packed (ccp) anion lattice with Li^+ occupying the remaining octahedral sites. The structure is built up of $[Mo_2O_{10}]$ clusters, consisting of edge sharing MoO_6 octahedra.[22,23] The hypothetical binary mixture between "Li_4MoO_5−Li_2NiTiO_4" forms a single phase solid solution with $Li_{1.2}Ni_{1/3}Ti_{1/3}Mo_{2/15}O_2$ stoichiometry and crystallizes in the α $LiFeO_2$ type structure, as illustrated in Figure 1a.

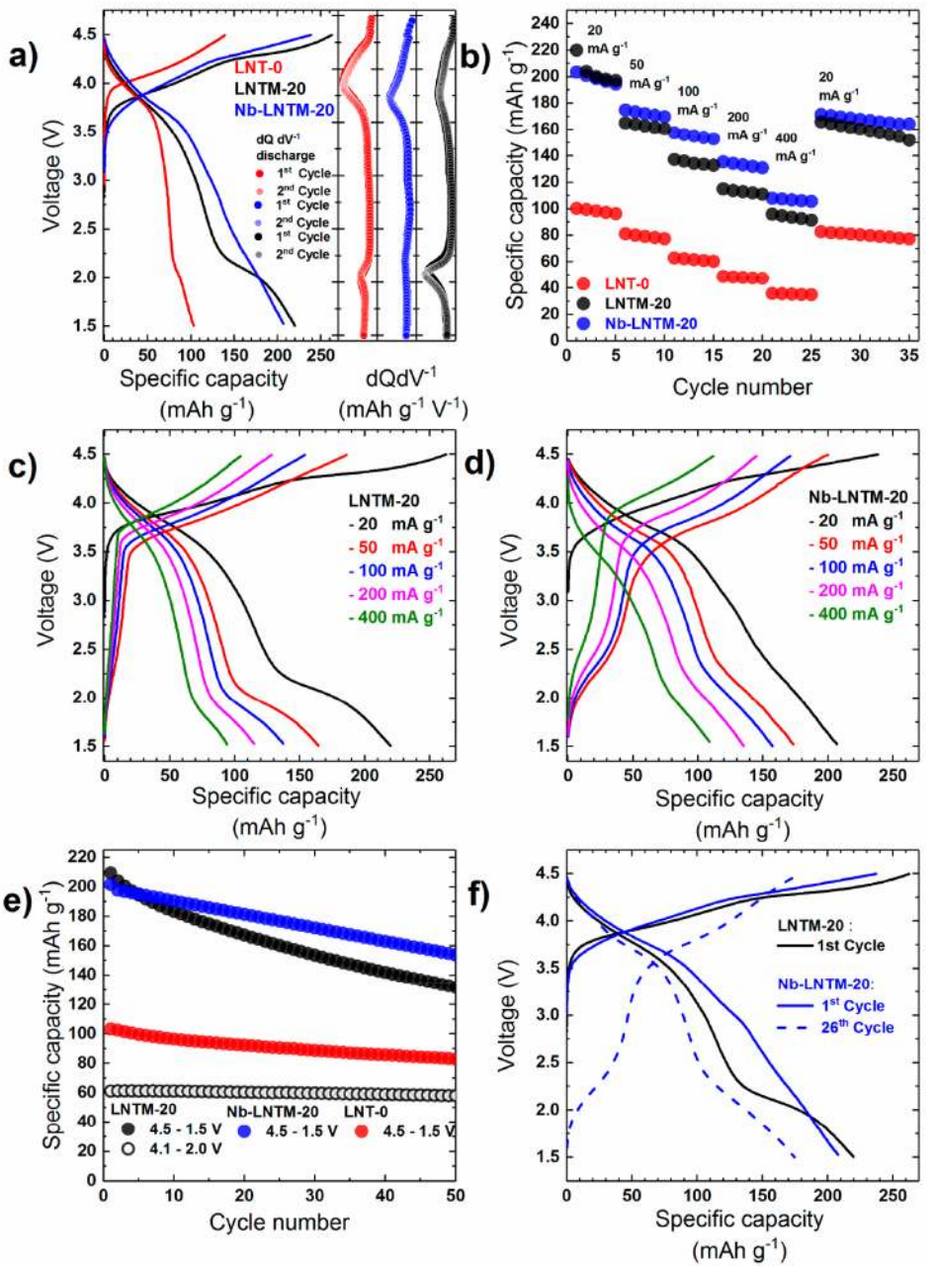

Figure 2. (a) Charge−discharge profiles of LNT 0, LNTM 20, and Nb LNTM 20 with the corresponding differential capacity plots of the discharge cycle at 20 mA g^{-1}. (b) Rate capability test for all compounds in the range of 4.5−1.5 V vs Li^+/Li. Voltage profiles of (c) LNTM 20 and (d) Nb LNTM 20 for different specific currents. (e) Cycling stability of all compounds for various cutoff voltages at 20 mA g^{-1}. (f) Charge−discharge profiles of LNTM 20 (1st cycle) and Nb LNTM 20 (1st and 26th cycles).

$Li_{1.2}Ni_{1/3}Ti_{1/3}Mo_{2/15}O_2$ has been synthesized and subsequently coated with 5 wt % $LiNbO_3$ on the pristine powder (see experimental details below). No evidence of the presence of a $LiNbO_3$ phase was found in the diffraction data of the $LiNbO_3$ coated $Li_{1.2}Ni_{1/3}Ti_{1/3}Mo_{2/15}O_2$. It has been shown that the metal oxide coating can react with the bulk material under high temperature treatment.[24,25] This leads to niobium substitution in this specific case. In the following, $LiNi_{0.5}Ti_{0.5}O_2$ is referred to as LNT 0, $Li_{1.2}Ni_{1/3}Ti_{1/3}Mo_{2/15}O_2$ as LNTM 20, and $LiNbO_3$ coated $Li_{1.2}Ni_{1/3}Ti_{1/3}Mo_{2/15}O_2$ as Nb LNTM 20. The number at the end of the abbreviation indicates the lithium excess. Rietveld refinement analysis of LNT 0, LNTM 20, and Nb LNTM 20 is shown in Figure S1a−c of the Supporting Information (SI). The refined lattice parameter for a single phase fit in *Fm*3*m* space group is a = 4.141830(21) Å for LNT 0, a = 4.146881(33) Å for LNTM 20, and a = 4.146980(24) Å for Nb LNTM 20. Nb LNTM 20 shows a slightly larger a lattice parameter, which is consistent with the larger cation radius of Nb^{5+}, compared to Ni^{2+} and Ti^{4+}. The chemical composition of the compounds has been determined by inductively coupled plasma optical emission spectroscopy (ICP OES) and is given in Table S1 (SI). Transmission electron microscopy (TEM) images are shown in Figure S2 (SI), depicting small spherical crystallites around 100 nm in diameter for LNT 0 and LNTM 20. For more insight into the coating, dark field scanning transmission

electron microscopy energy dispersive X ray spectroscopy (STEM EDX) mapping of Nb LNTM 20 was carried out. The corresponding maps of O, Ni, Ti, Mo, and Nb are shown in Figure 1b,c. The Nb signal was found throughout the particle, with an increasing intensity from the center toward the edge. This indicates some Nb segregation to the outer surface. The combined X ray diffraction (XRD) and STEM EDX data suggest partial incorporation of Nb into the Li−Ni−Ti−Mo bulk lattice. A line scan along a crystallite grain confirms a Nb rich outer surface layer of varying thickness (up to 12 nm). We estimate that ∼47% of the Nb is substituted into the phase, leading to a nominal stoichiometry of $Li_xNi_{0.328}Ti_{0.328}Mo_{0.131}Nb_{0.016}O_2$. X ray photoelectron spectroscopy (XPS) results in Figure S3 (SI) indicate that Nb is in the +5 oxidation state.

Electrochemical Properties. The electrochemical properties were analyzed by galvanostatic charge−discharge measurements. Figure 2a shows the charge−discharge profiles for LNT 0, LNTM 20, and Nb LNTM 20 half cells. The samples were cycled in the voltage range of 4.5−1.5 V vs Li^+/Li using a constant specific current of 20 mA g^{-1}. The specific discharge capacity increased significantly from 100 to 220 mAh g^{-1} upon changing from stoichiometric LNT 0 to Li rich LNTM 20. This increase in accessible capacity agrees with expectations based on percolation theory.[10,11,26] The latter predicts that the 0 TM site can percolate and form extended lithium networks with 9% excess lithium, thus allowing more lithium to be intercalated/deintercalated. For Nb LNTM 20, the voltage profile changed compared to that of the pristine sample. This is obvious from the corresponding differential capacity curves. Remarkably, Nb LNTM 20 showed a longer and more defined upper voltage plateau and higher capacity contribution in the high voltage regime >2.5 V than LNTM 20. LNTM 20 showed an overall higher initial specific discharge capacity. However, a significantly higher fraction of the capacity is gained in the low voltage regime (<2.5 V), accompanied by a low voltage plateau around 2.2 V. In order to assess the influence of particle size on the accessible specific capacity, the sintering time was varied. The average particle sizes of LNTM 20 sintered for 2 and 4 h and Nb LNTM 20 sintered for 4 h were 96, 220, and 176 nm, respectively, as shown in Figure S4a−c. LNTM 20 with an average particle size of 220 nm displayed a much lower specific discharge capacity of 170 mAh g^{-1} as compared to LNTM 20 with an average size of 96 nm (Figure S5, SI), indicating a particle size dependence of the accessible capacity. This points to diffusion limitations. Figure 2b illustrates the rate performance of all compounds, which involved five consecutive cycles at a constant specific current. At higher currents, Nb LNTM 20 retained more of the capacity than both LNT 0 and LNTM 20. For specific currents of 20, 50, 100, 200, and 400 mA g^{-1}, Nb LNTM 20 exhibited specific capacities of 200, 174, 157, 135, and 108 mAh g^{-1}, whereas for LNTM 20 the corresponding values were 220, 164, 137, 115, and 95 mAh g^{-1}. For specific currents >50 mA g^{-1}, Nb LNTM 20 showed higher discharge capacities. The respective first cycle charge−discharge profiles for each current step are shown for both LNTM 20 and Nb LNTM 20 in Figure 2c,d. For higher currents, we observed an increase in polarization and a decrease in the specific capacity. Figure 2e shows the cycling stability of the investigated electrode materials. Nb LNTM 20 demonstrated better capacity retention compared with LNTM 20. The better rate capability, in conjunction with the improved cycling stability, further highlights the importance of surface modification. Low capacity retention for Li rich rock salt oxides is a widely observed phenomenon.[8,27,28] It is believed to originate from the participation of anions in the charge compensation process (oxygen redox/release), as discussed below. Note that the charge−discharge profiles for Nb LNTM 20 in the later cycles reveal the appearance of a low voltage plateau and the voltage profile resembles the behavior of LNTM 20, as shown in Figure 2f. With prolonged cycling, the voltage hysteresis increased along with an increased capacity contribution from the low voltage region <2.5 V. Furthermore, the cycling stability of LNTM 20 appears to depend on the charge cutoff voltage, showing severe degradation when charged to high potentials. Being charged to high potentials, the Li rich DRS can exhibit irreversible phenomena like oxygen evolution from the surface and side reactions.[27] The first cycle oxygen release for LNTM 20 is believed to cause cation densification and structural reconstruction of the surface phase, thereby impeding Li conductivity and leading to impedance buildup. The observed plateau around 2.2 V has been related to surface densification after oxygen loss.[18,29] For Nb LNTM 20, this plateau is greatly reduced. Thus, surface modification seems to be beneficial in protecting the reactive surface and impeding surface densification.[30] For a relatively narrow voltage window of 4.1−2.0 V, oxygen evolution or oxygen participation can be suppressed, and better cycling stability is achieved. This will be discussed in the following sections. Cycling LNTM 20 in a smaller voltage window leads to more symmetric profiles with lower voltage hysteresis, as shown in Figure S6 (SI). Nb LNTM 20 was subjected to milling in organic solvent and sintering as additional processing steps, which may affect its electrochemistry. In order to elucidate the influence of such additional steps on the electrochemistry, LNTM 20 was processed in the same way, without the addition of lithium and niobium precursors. The resulting charge−discharge profile is presented in Figure S7a and the rate capability test shown in Figure S7b of the SI. The processed LNTM 20 showed a slightly lower specific capacity and a larger hysteresis, possibly due to lithium leaching during the solvent treatment.

As mentioned above, we hypothesize that the surface phase evolution is indicated by the appearance of the low voltage plateau ∼2.2 V. For the modified compound, the first discharge does not reveal any visible low voltage plateau, which only appears with higher cycle numbers, as shown in Figure 2f. On the contrary, the unmodified sample shows already in the first discharge a visible low voltage plateau from which we inferred that the surface phase evolution is mitigated for Nb LNTM 20. Electrochemical impedance spectra were measured to gain a better understanding of the improved cycling performance. Figure 3 shows the ac impedance spectra (Nyquist plots) of pristine LNTM 20 and of surface modified Nb LNTM 20, measured after 2 and 40 cycles for the discharged state. The equivalent circuit[31] is shown in the inset, and the fitting results are listed in Table S2 (SI). The spectra exhibit two semicircles at high and low frequencies and a Warburg tail at very low frequencies. The first, potential independent semicircle is attributed to the surface processes, e.g., the resistance of Li^+ migration through electrode surface films (surface film resistance R_1). The second, potential dependent semicircle reflects the charge transfer (interfacial) resistance R_2.[32] The Warburg tail is ascribed to the diffusion of Li ions into the electrode material (Warburg element). Both materials (pristine and Nb coated) show a similar starting behavior and display

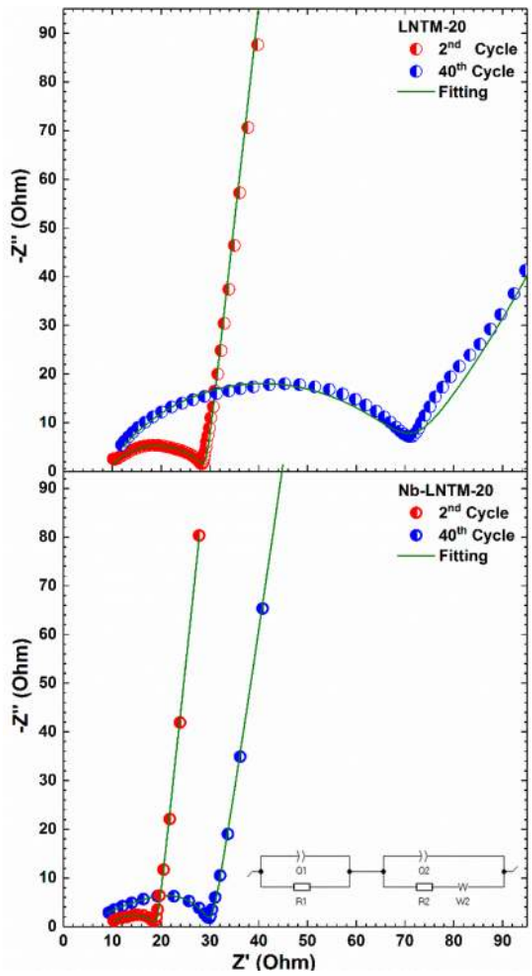

Figure 3. Impedance spectra obtained for the discharged state (1.5 V) after the 2nd and 40th cycles, respectively, on (a, top) LNTM 20 and (b, bottom) Nb LNTM 20. The corresponding equivalent circuit is shown in the inset.

growth in impedance with electrochemical cycling. The charge transfer resistances "R_2" of the pristine and surface modified cathode after the 2nd and 40th cycles have been compared. R_2 is 20 and 67 Ω for the pristine cathode, and 8 and 23 Ω for the surface modified compound, respectively. During prolonged cycling, the charge transfer resistance significantly increases for the pristine cathode (by 44 vs 16 Ω for the surface modified cathode). The increase in charge transfer resistance is tentatively attributed to structural changes on the surface. These results demonstrate that the surface modified compound shows a relatively low impedance after oxygen loss as compared to pristine material. However, the increase in impedance with cycling is significant, in accordance with the continuing capacity fading seen for Nb LNTM 20.

The electrode kinetics depend on both the ion transport and electronic conductivity and can limit the overall performance. The total conductivity of LNT 0 and LNTM 20 was studied by ac impedance spectroscopy at various temperatures, as shown in Figures S8 and S9 of the SI. The activation energy (E_a) was calculated via the Arrhenius equation, from the slope of ln σ vs T^{-1}, where σ is the conductivity and T represents the absolute temperature. LNTM 20 shows a higher room temperature conductivity of $\sim 3.0 \times 10^{-6}$ S cm^{-1} compared to LNT 0 ($\sim 7.1 \times 10^{-8}$ S cm^{-1}). The donation of d electrons from Mo to the conduction band can explain the increase in conductivity for LNTM 20. The activation energy (E_a) for LNT 0 (319 ± 19 meV) is higher than for LNTM 20 (249 ± 16 meV). Overall, the conductivity is sufficiently high so that no electronic limitations are to be expected. Important to mention is that, with the state of charge and the number of cycles, the conductivity can vary by several orders of magnitude.[33]

For lithium rich materials, both oxygen redox and lattice oxygen loss upon cycling are well known phenomena.[34,35] In order to find out whether oxygen release takes place in the case of overlithiated LNTM 20, in situ differential electrochemical mass spectrometry (DEMS) measurements were conducted and the results compared to LNT 0, which served as reference material. To this end, half cells were charged at C/10 to 4.5 V (1C = 210 mA g^{-1} for LNTM 20 and 100 mA g^{-1} for LNT 0) while monitoring gas evolution. As depicted in Figures 4 and S10 (SI), the LNTM 20 and LNT 0 half cells showed first cycle charge capacities of 157 and 88 mAh g^{-1}. The specific capacities were lower for the thicker electrodes used in the DEMS measurements. CO_2 evolution was observed, starting around 3.9 V for LNTM 20 and 4.1 V for LNT 0. The quantities detected for LNTM 20 were below 2 ppm up to 4.1 V (50 mAh g^{-1}), thus making a precise determination of the onset potential difficult. As expected, significant oxygen release was only observed for the overlithiated material, starting at 4.4 V. This is indicative of lattice changes during cycling operation, eventually leading to an oxygen deficient (surface) structure.

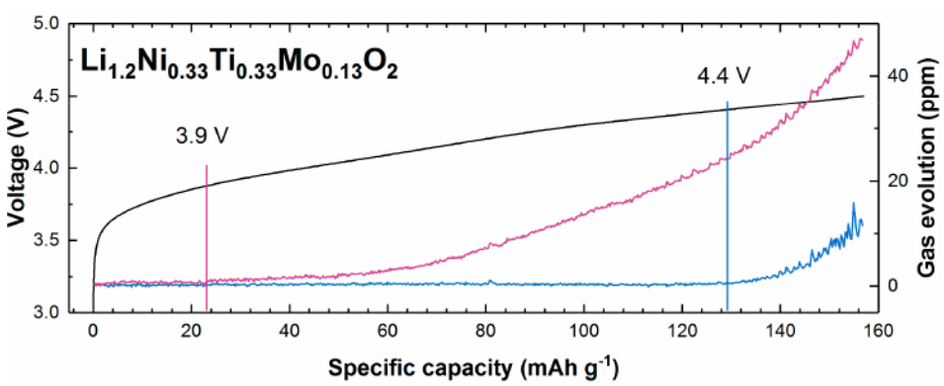

Figure 4. DEMS measurements of the first charge cycle at C/10 to 4.5 V for LNTM 20 half cells. The cell voltage (black) is shown together with the O_2 (blue) and CO_2 (red) evolution.

Chemical reactions of released oxygen with the electrolyte are not the only source of CO_2 evolution, as both materials show similar behavior. Electrochemical electrolyte oxidation[36,37] and decomposition of residual carbonate[38,39] species from the synthesis, for instance, may also account for the CO_2 evolution.

Structural Changes upon Cycling. In situ XRD measurements were carried out to investigate the structural changes of LNTM 20 during two consecutive cycles between 4.5 and 1.5 V at C/30. The voltage profile and the changes in the *a* lattice parameter from single phase XRD refinement are shown in Figure 5, with an enlarged section displaying the

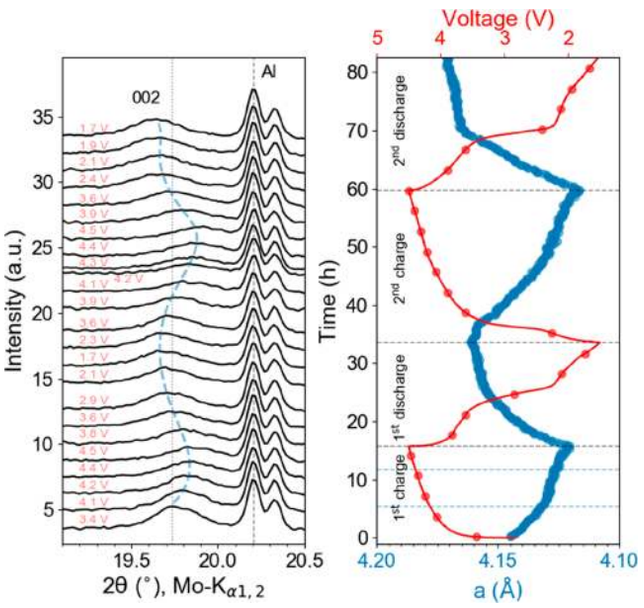

Figure 5. (left) In situ XRD pattern of LNTM 20 for two consecutive cycles in the range of 4.5−1.5 V at C/30. (right) Corresponding voltage profile and changes in the *a* lattice parameter from Rietveld refinement analysis. The red curves are the voltage profile and the red dots the measurement points, where the XRD patterns were collected.

pattern around the 002 reflection. During the first charge, three regimes can be seen. The first charge regime until 4 V reveals a sloped voltage profile, where the *a* lattice parameter is continuously decreasing, thus reflecting lattice contraction. This finding can be associated with a $Ni^{2+/3+}$ oxidation process [Ni^{2+} (r = 0.69 Å) and Ni^{3+} (r = 0.56 Å)]. The second regime is along the 4.3 V plateau, where the lattice parameter changes only slightly, and the third regime occurs toward the end of the charge, where the lattice parameter is continuously decreasing. This result can be attributed to oxygen oxidation and then release. In the midregime, the lattice parameter is only changing in the beginning and at the end of charge. We argue that oxygen (O^{2-}) oxidation is associated with a shrinkage of the oxygen framework because of the smaller size of the oxygen anion or due to the formation of peroxo like species with shorter oxygen−oxygen bonds.[40] During the first discharge, the lattice parameter continuously increases (lattice expansion) until 2.2 V. Further discharge affects the lattice only slightly. During the second cycle upon discharge, a more pronounced plateau is observed for voltages <2.2 V, with only slight changes in the *a* lattice parameter.

Redox Mechanism. Further information on the redox mechanism of LNTM 20 and LNT 0 was obtained from X ray absorption near edge structure (XANES) measurements. Figure S11a (SI) shows the Ni K edge spectra of pristine LNT 0 after charging to 4.5 V and then discharging to 1.5 V. Comparison of LNT 0 with a NiO reference compound reveals that the edge energy is similar, indicating that the Ni oxidation state is +2. Figure 6a shows similar results for LNTM 20.

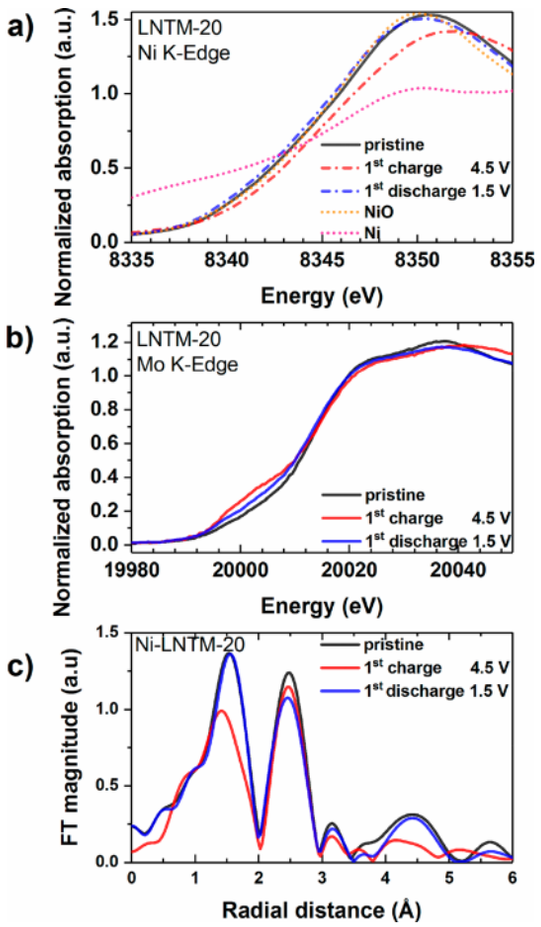

Figure 6. (a) XANES Ni K edge spectrum for LNTM 20 and (b) Mo K edge spectrum for LNTM 20. (c) FT EXAFS of Ni.

During charging, the Ni K edge shifted significantly to higher energies, thereby reflecting an increase in oxidation state. On the basis of Faraday's law, the theoretical capacities for different redox processes have been calculated and are listed in Table 1. The oxidation state of Ti was determined by XPS to be +4, as shown in Figure S12 (SI). Ti^{4+} was fully oxidized and therefore assumed to be electrochemically inactive.[41,42] Note that neither XANES nor XPS can rule out the formation of small amounts of Ti^{3+}, in the atom percent range. The

Table 1. Theoretical Specific Capacity for Different Valence Changes and the Specific Lithium Capacity of LNT 0 and LNTM 20

	theoretical capacity/mAh g^{-1}				
compound	$Ni^{2+/3+}$	$Ni^{2+/4+}$	Mo^{n+1}	Mo^{n+2}	Li specific capacity
$LiNi_{1/2}Ti_{1/2}O_2$ (LNT-0)	144	287			287
$Li_{1.2}Ni_{1/3}Ti_{1/3}Mo_{2/15}O_2$ (LNTM-20)	101	202	40	80	364

measured specific capacity for each state of charge can be used to estimate the average valence change.

For LNT 0, the specific capacities for charging to 4.5 V and subsequently discharging to 1.5 V were 145 and 106 mAh g^{-1}, respectively. This corresponds to 0.5 Li extraction and 0.37 Li intercalation per formula unit (fu), which can be attributed to the Ni^{2+}/Ni^{3+} redox couple. Interestingly, LNTM 20 delivered 262 mAh g^{-1} during charge, corresponding to 0.86 Li per fu, which is beyond the theoretical capacity for the $Ni^{2+/4+}$ redox couple with 202 mAh g^{-1}. This suggests that more redox active species are involved in the reaction, although electrolyte/electrode side reactions can also be expected. As confirmed by DEMS, O_2 evolution takes place during charge, and therefore, oxidation of O^{2-} must be considered as an additional mechanism for charge compensation. For the consecutive discharge to 1.5 V, LNTM 20 exhibited a specific discharge capacity of 212 mAh g^{-1}, corresponding to 0.73 Li per fu. Simultaneously, the Ni K edge shifts back to lower energies, pointing to nickel reduction. In Figure S11b (SI), the comparison between the Ni K edge of LNT 0 and LNTM 20 in the charged state shows similar edge energies, suggesting that Ni is in the oxidation state +3 in both cases. In conclusion, oxidation to Ni^{4+} can be excluded for LNTM 20, limiting the nickel redox contribution to $Ni^{2+/3+}$. Interesting to note is that the pre edge peak intensity of Mo increased significantly after the first charge and remained at a higher value after the discharge, which is shown in Figure 6b. This finding indicates an increased distortion of the MoO_6 octahedra compared to the pristine state. The intensities for these transitions are very sensitive to the coordination environment and the symmetry of the metal center. For centrosymmetric symmetry, the pre edge is weak, as it is limited by a weak electric quadrupole intensity mechanism.[43] This pre edge structure is typically observed for α MoO_3 with Mo in the oxidation state +6. The increase in pre edge peak, with the shift of the white line to higher energies, suggests oxidation of Mo upon charging.[44] On the basis of the results of a linear combination fit, the initial bulk oxidation state of Mo is estimated to be +4.7 and increases to around +6 upon charging. During discharge, it decreases to +3.2.

XANES in fluorescence mode is a method to probe the bulk and investigate the average oxidation state; however, it is not sensitive to changes in the surface or near surface range. As evidenced by DEMS, O_2 release takes place. Therefore, XPS was used to characterize the surface oxidation state for the charged material, as shown in Figure S12 (SI). Note that a mixed oxidation state with mainly +6 and a minority at +4 is found for Mo. The partial reduction of Mo at the surface is possibly promoted after the oxygen loss.[45,46] We did not observe any changes in the oxidation state of Ti. By charge balancing, we can roughly estimate the oxygen redox contribution to the total (reversible) capacity. On the basis of the derived oxidation states, Mo contributes with 52 mAh g^{-1} to the total specific charge capacity, without any contribution of the fully oxidized Ti^{4+}. Assuming that during charging Ni is oxidized to +3, the $Ni^{2+/3+}$ redox reaction can account for 101 mAh g^{-1}. The remaining charge capacity must be compensated by oxygen anions, with an estimated contribution of 109 mAh g^{-1} during the first charge cycle.

The local environment of the Ni ions in LNT 0 and LNTM 20 was investigated by extended X ray absorption fine structure (EXAFS) measurements. Figures 6c and S11c (SI) depict the Fourier transformed (FT) spectra of the Ni K edge for different states of charge. The first coordination shell (Ni−O) reflects the contribution of oxygen, while the second one is related to backscattering from Ni ions (Ni−Ni). The most notable change takes place in the first coordination shell during charge, indicating that the charge compensation results in lower Ni−O peak amplitude. Ni^{3+} in the low spin state is expected to result in a Jahn−Teller distortion, which is increased by oxidation. This leads to a decrease in the amplitude of the Ni−O peak.[47] The shape of the first coordination shell reveals the existence of two Ni−O peaks, suggesting distorted octahedral coordination. In Figure 6c, the amplitude R decreases for the first charge due to the change in the coordination environment and completely recovers after the first discharge. In the case of LNT 0, in Figure S11c (SI), the amplitude R for the first discharge increases compared to that of the pristine state, suggesting that the pristine material partially contains Ni^{3+}, which is being reduced during the first discharge.

DISCUSSION AND CONCLUSIONS

Li rich cation disordered rock salt oxides have promising properties, such as high capacity. Furthermore, they allow for a large number of element combinations, which can be favorable in terms of sustainability and cost. However, challenges have to be overcome in order to achieve viable systems. So far, extended cycling stability with little capacity fading has not been demonstrated yet. In addition, problems hindering practical applications like voltage hysteresis and poor rate capability still need to be addressed and resolved. With increasing lithium excess, new redox processes—which include oxygen activity—can be expected. Disadvantages of this process are the associated oxygen release, leading to surface degradation, side reactions with the electrolyte, cation densification, and overall performance degradation. In particular, higher resistances lead to lower rate capability. DEMS measurements provided clear evidence that O_2 is released for Li rich LNTM 20, but not for stoichiometric LNT 0.

In order to alleviate the above mentioned drawbacks, approaches comprising both structural and surface/interface modifications have been intensively studied.[30,31] Recently, Lee et al.[29] demonstrated that substitution of oxygen by fluorine could mitigate oxygen loss and improve the cycling stability of the Li rich Li−Ni−Ti−Mo−(O/F) system. The fluorine substitution is an effective way to enable an introduction of lithium excess in low valent systems without the use of heavy high valent charge compensators, which can lower the specific capacity. Practically, this approach aims to increase the cationic redox capacity. Fluorine doping has been reported to mitigate oxygen loss, improve capacity retention, and increase the average voltage in some examples.[18,48] However, stronger interactions between lithium and fluorine and lithium migration into tetrahedral sites for a high states of charge impose constraints to the accessible capacity.[49] Another interesting approach shown by Shin et al.[50] could experimentally demonstrate that oxygen loss can be mitigated by low level doping of heavy elements such as Ta, resulting in surface modification. The improvement has been rationalized by the enhanced oxygen retention of Ta and the tendency of heavy elements to segregate at the surface due to their larger ionic radii.

Our approach targets the surface modification and physical protection through a ceramic coating in order to mitigate the

surface phase evolution, which leads to performance degradation.

Here, we propose an approach comprising a surface treatment with $LiNbO_3$ in order to improve the electrochemical performance of the material. Unmodified $Li_{1.2}Ni_{0.333}Ti_{0.333}Mo_{0.133}O_2$ showed a high specific capacity but displayed a significant polarization for high degrees of delithiation (~4.3 V). The $LiNbO_3$ modified $Li_{1.2}Ni_{0.333}Ti_{0.333}Mo_{0.133}O_2$, on the other hand, showed less polarization, with a higher average discharge voltage and a significantly higher capacity contribution in the high voltage regime. We argue that the change of the voltage profile can be attributed to the formation of a Li−Ni−Ti−Mo−Nb solid solution due to partial interdiffusion of cations from the surface coating into the active material during sintering. This observation is reflected in the lower impedance growth of Nb LNTM 20 during cycling. We suggest that the lower charge transfer resistance and impedance increase for the surface modified compound can be attributed to the mitigated surface densification. For further optimization, a uniform coating is required. In addition, the influence of sintering temperature on the interdiffusion mentioned above needs to be better understood. Alternatively, $LiTaO_3$ is a possible candidate compound that could be used for the surface modification, since Ta doping in a disordered rock salt has been shown to affect the surface chemistry due to segregation of the heavy element dopant on the surface, thereby mitigating oxygen loss.[50]

In summary, we have demonstrated that high delithiation of $Li_{1.2}Ni_{0.333}Ti_{0.333}Mo_{0.133}O_2$ triggers oxygen release, resulting in substantial performance decay. The changes in oxidation state, bond distance, and coordination environment for different states of charge are illustrated. XANES spectroscopy revealed that Ni is oxidized from +2 to +3. At the same time, Mo changes its oxidation state from the pristine state with +4.7 to around +6 in the charged state; it is reduced to +3.2 in the consecutive discharge cycle.

Furthermore, an irreversible structural distortion of the Mo environment was observed upon cycling. XPS revealed that in the charged state, Mo has a mixed oxidation state on the surface, with predominantly +6 and +4. Thus, in the fully charged state, we estimate that 109 mAh g^{-1} (around 0.36 Li per formula unit) are charge compensated by oxygen anion oxidation, triggering O_2 evolution, accompanied by partial reduction of Mo to +4 near the surface.

Moreover, a strong particle size dependence of the accessible discharge capacity indicates the necessity of using small size material for achieving high specific capacities. To the best of our knowledge, this is the first time a surface modification using the solid state electrolyte $LiNbO_3$ has been tested for cation disordered rock salt oxides. The voltage hysteresis was significantly reduced for Nb LNTM 20 over LNTM 20. This observation was reflected by the lower impedance and also the relatively lower impedance buildup as compared to the pristine material. Overall, we conclude that surface modifications hold promise to further improve the rate capability and cycling performance of Li rich cation disordered rock salt oxides.

■ EXPERIMENTAL SECTION

Synthesis. The procedure to synthesize $LiNi_{0.5}Ti_{0.5}O_2$ and $Li_{1.2}Ni_{1/3}Ti_{1/3}Mo_{2/15}O_2$ was adopted from Lee et al.[29] Li_4MoO_5 was synthesized using modified conditions. Li_2CO_3 (Alfa Aesar, >99%), $NiCO_3$ (Alfa Aesar, 99%), TiO_2 nanopowder (<50 nm particle size, Alfa Aesar, 99.7%), and MoO_2 (Alfa Aesar, 99%) were employed as the precursors. Other than for $LiNi_{0.5}Ti_{0.5}O_2$, stoichiometric amounts of precursors were used. For $Li_{1.2}Ni_{1/3}Ti_{1/3}Mo_{2/15}O_2$ and Li_4MoO_5, 5% excess of Li was used. The precursors were ball milled for 24 h with 200 rpm using a Fritsch P6 planetary ball mill with a 80 mL silicon nitride vial and silicon nitride balls, with a ball to powder weight ratio of 20:1. The mixture of the precursors was pelletized and then sintered at 750 °C for 2 h in air, followed by furnace cooling to 200 °C and immediate transfer inside an argon filled glovebox. Li_4MoO_5 was sintered at 900 °C for 2 h. After sintering, the pellets were manually ground into a fine powder.

For coating, we prepared a solution between solid lithium ethoxide (Sigma Aldrich, 95%) and liquid niobium isopropoxide solution (Alfa Aesar, 99%, 10 wt % niobium isopropoxide in 50:50 (v:v) 2 propanol/hexane) with a nominal stoichiometry of 1.05:1.0 of Li to Nb. $Li_{1.2}Ni_{1/3}Ti_{1/3}Mo_{2/15}O_2$ was ball milled with the prepared coating solution using a Fritsch P9 with a 15 mL vial volume for 12 h at 200 rpm (ball to powder ratio of 15:1). Subsequently, the mixture was dried overnight in an oven in an argon filled glovebox and then pelletized and sintered at 400 °C for 2 h in air, followed by furnace cooling to 200 °C and immediate transfer into an argon filled glovebox. After the sintering, the pellets were manually ground into a fine powder.

Electrochemical Measurements. Electrochemical tests were carried out in a Swagelok type cell using Li foil as the counter electrode. Electrode slurries were made of 90 wt % composite and 10 wt % polyvinylidene difluoride (PVDF) binder with *N* methyl 2 pyrrolidone (NMP) as the solvent. The composite consists of active material and Super C65 carbon black in a weight ratio of 80:20. The mixed slurry was coated on an aluminum foil using the doctor blade technique and dried at 120 °C for 12 h under vacuum. Each working electrode (12 mm diameter) contained about 3 mg of active material. LP30 from BASF (ethylene carbonate/dimethyl carbonate, 1:1 weight ratio with 1 M $LiPF_6$) was used as the electrolyte. Galvanostatic charge−discharge experiments were conducted at 25 °C in a climate chamber using an Arbin electrochemical workstation.

Impedance Spectroscopy. For a better understanding of the cycling performance of surface modified Nb LNTM 20 relative to pristine LNTM 20, electrochemical impedance spectra were measured at 25 °C after the 2nd and 40th cycles. Electrochemical impedance spectroscopy (EIS) was performed using a three electrode PAT Cell (EL CELL) with a Li ring as the reference electrode and Li metal (18 mm) as the counter electrode. The working electrode size was 18 mm, and aluminum served as the current collector. The experiments were conducted using a Bio Logic electrochemical workstation with an applied sinusoidal excitation voltage of 10 mV in the frequency range between 200 kHz and 0.1 Hz.

Differential Electrochemical Mass Spectrometry. In situ gas analysis was performed by use of differential electrochemical mass spectrometry (DEMS). The setup has been described elsewhere.[37,51] Custom cells with gas inlets and outlets were assembled in an argon filled glovebox. The cathodes used (40 mm diameter with a 4 mm hole for proper gas extraction) had areal loadings of about 1 mg_{LNT-0}/cm^2 and 1.6 $mg_{LNTM-20}/cm^2$. GF/A (42 mm diameter, GE Healthcare Life Sciences, Whatman) was used as the separator, 600 μL of LP47 (1 M $LiPF_6$ in ethylene carbonate/diethyl carbonate, 3:7 by weight, BASF) as the electrolyte, and 600 μm thick Li metal foil (Albemarle Germany GmbH) with a diameter of 40 mm as the counter electrode. A constant carrier gas flow (2.5 mL_{He}/min, purity 6.0) was applied during DEMS measurements for gas extraction. The gas was analyzed via mass spectrometry (GSD 320, OmniStar Gas Analysis System, Pfeiffer Vacuum GmbH). After each run, a calibration gas of known composition was introduced to quantify the measured ion currents.

Conductivity. To measure the conductivity, powder materials were pressed into pellets with a diameter of 8 mm and coated with a gold layer on both sides by sputtering. The ac impedance data were collected in the frequency range from 0.1 Hz to 1 MHz (10 mV_{rms} amplitude) using a frequency response analyzer (ZAHNER Elektrik GmbH) at various temperatures (25−80 °C). After each temperature, the samples were allowed to equilibrate for a substantial amount of

time. The impedance data were fitted and analyzed using the ZMAN 2 software.

X-ray Absorption Spectroscopy. The P65 XAS beamline (PETRA III, Hamburg) provides a relatively large beam (0.5 × 1 mm^2) and a moderate photon flux density. The 11 period mini undulator delivers a monochromatic photon flux of about 10^{11} ph/s. Two plane mirrors with variable angle of incidence and three different surface coatings were installed in front of the water cooled double crystal monochromator. Si(111) and Si(311) crystals were used for the energy ranges of 4−22 and 7−44 keV, respectively. The P65 beamline is also equipped with a 7 pixel HPGe energy dispersive detector and Si PIPS diode. X ray absorption spectroscopy measure ments were performed in both transmission and fluorescence modes. For ex situ measurements, the step scan mode with a duration of about 10−11 min for each spectrum was used. The spectra were processed using the Demeter software package based on IFEFFIT and FEFF.[52]

X-ray Diffraction. In situ X ray diffraction (XRD) patterns were collected using modified coin cells on a parallel beam laboratory diffractometer with a microfocus rotating anode (Mo Kα radiation) in transmission geometry and a Pilatus 300 K W area detector. The coin cells comprise an LNTM 20 based cathode, a Li metal anode, and a Whatman glass fiber separator. The electrolyte was 1 M $LiPF_6$ in ethylene carbonate:dimethyl carbonate 1:1 (w:w) from BASF. Galvanostatic charge−discharge cycling was performed with an Ivium potentiostat between 1.5 and 4.5 V at 10 mA g^{-1}. Diffraction patterns were collected every 300 s. Two consecutive patterns were added up to eliminate cosmic spikes on the detector. The diffraction images were integrated using the pyFAI software[53] and analyzed with the Rietveld method using TOPAS V6.

X-ray Photoelectron Spectroscopy. The elemental composi tion of the surface region was analyzed by X ray photoelectron spectroscopy (XPS) using a Physical Electronics PHI 5800 ESCA system. The measurements were carried out with monochromatic Al Kα radiation (250 W, 13 kV) at a detection angle of 45° and with pass energies of 93.9 and 29.35 eV for survey and detail measurements, respectively. An electron flood gun was used for sample neutralization. The main C 1s peak was set to 284.8 eV for binding energy calibration. Some samples were subject to Ar^+ sputtering (sputter rate ∼1 nm min^{-1}, 1 mA, 5 kV) to remove the topmost surface layer.

Transmission electron microscopy. Transmission electron microscopy (TEM) investigations were performed on a Tecnai F20ST transmission electron microscope operated at 200 kV. Samples for the TEM study were prepared using an FEI STRATA dual beam focused ion beam (FIB)/scanning electron microscope. The FIB lift out samples were milled using a Ga ion beam at 30 kV.

AUTHOR INFORMATION

Corresponding Author

*E mail: m.fichtner@kit.edu.

Musa Ali Cambaz: 0000 0002 4249 3486
Bhaghavathi P. Vinayan: 0000 0001 6491 5160
Torsten Brezesinski: 0000 0002 4336 263X
R. Jürgen Behm: 0000 0002 7565 0628
Helmut Ehrenberg: 0000 0002 5134 7130

Notes

The authors declare no competing financial interest.

ACKNOWLEDGMENTS

Financial support from the FET OPEN project "LiRichFCC" of the European Commission (grant agreement #711792) is gratefully acknowledged. This work contributes to the research performed at CELEST (Center for Electrochemical Energy Storage Ulm Karlsruhe). We want to thank Dr. Edmund Welter from Experiments Division XAS of PETRA III, Hamburg, Germany. This work is partially carried out with the support of the Karlsruhe Nano Micro Facility.

REFERENCES

(1) Scrosati, B.; Hassoun, J.; Sun, Y. K. Lithium Ion Batteries. A Look into the Future. *Energy Environ. Sci.* **2011**, *4* (9), 3287.

(2) Myung, S. T.; Maglia, F.; Park, K. J.; Yoon, C. S.; Lamp, P.; Kim, S. J.; Sun, Y. K. Nickel Rich Layered Cathode Materials for Automotive Lithium Ion Batteries: Achievements and Perspectives. *ACS Energy Lett.* **2017**, *2* (1), 196−223.

(3) Etacheri, V.; Marom, R.; Elazari, R.; Salitra, G.; Aurbach, D. Challenges in the Development of Advanced Li Ion Batteries: A Review. *Energy Environ. Sci.* **2011**, *4* (9), 3243.

(4) Zheng, J.; Myeong, S.; Cho, W.; Yan, P.; Xiao, J.; Wang, C.; Cho, J.; Zhang, J. G. Li and Mn Rich Cathode Materials: Challenges to Commercialization. *Adv. Energy Mater.* **2017**, *7* (6), 1601284.

(5) Sun, Y. K.; Myung, S. T.; Park, B. C.; Prakash, J.; Belharouak, I.; Amine, K. High Energy Cathode Material for Long Life and Safe Lithium Batteries. *Nat. Mater.* **2009**, *8* (4), 320−324.

(6) Hy, S.; Liu, H.; Zhang, M.; Qian, D.; Hwang, B. J.; Meng, Y. S. Performance and Design Considerations for Lithium Excess Layered Oxide Positive Electrode Materials for Lithium Ion Batteries. *Energy Environ. Sci.* **2016**, *9* (6), 1931−1954.

(7) Lu, Z.; Dahn, J. R. Understanding the Anomalous Capacity of $Li/Li[Ni_xLi_{(1/3-2x/3)}Mn_{(2/3\ x/3)}]O_2$ Cells Using In Situ X Ray Diffraction and Electrochemical Studies. *J. Electrochem. Soc.* **2002**, *149* (7), A815−A822.

(8) Koga, H.; Croguennec, L.; Menetrier, M.; Douhil, K.; Belin, S.; Bourgeois, L.; Suard, E.; Weill, F.; Delmas, C. Reversible Oxygen Participation to the Redox Processes Revealed for $Li_{1.20}Mn_{0.54}Co_{0.13}Ni_{0.13}O_2$. *J. Electrochem. Soc.* **2013**, *160* (6), A786−A792.

(9) Rozier, P.; Tarascon, J. M. Review—Li Rich Layered Oxide Cathodes for Next Generation Li Ion Batteries: Chances and Challenges. *J. Electrochem. Soc.* **2015**, *162* (14), A2490−A2499.

(10) Lee, J.; Urban, A.; Li, X.; Su, D.; Hautier, G.; Ceder, G. Unlocking the Potential of Cation Disordered Oxides for Recharge able Lithium Batteries. *Science (Washington, DC, U. S.)* **2014**, *343* (6170), 519−522.

(11) Urban, A.; Lee, J.; Ceder, G. The Configurational Space of Rocksalt Type Oxides for High Capacity Lithium Battery Electrodes. *Adv. Energy Mater.* **2014**, *4* (13), 1400478.

(12) Yabuuchi, N.; Takeuchi, M.; Nakayama, M.; Shiiba, H.; Ogawa, M.; Nakayama, K.; Ohta, T.; Endo, D.; Ozaki, T.; Inamasu, T.; et al. High Capacity Electrode Materials for Rechargeable Lithium Batteries: Li_3NbO_4 Based System with Cation Disordered Rocksalt Structure. *Proc. Natl. Acad. Sci. U. S. A.* **2015**, *112* (25), 7650−7655.

(13) Yabuuchi, N.; Nakayama, M.; Takeuchi, M.; Komaba, S.; Hashimoto, Y.; Mukai, T.; Shiiba, H.; Sato, K.; Kobayashi, Y.; Nakao, A.; et al. Origin of Stabilization and Destabilization in Solid State

Redox Reaction of Oxide Ions for Lithium Ion Batteries. *Nat. Commun.* **2016**, *7*, 13814.
(14) Fell, C. R.; Qian, D.; Carroll, K. J.; Chi, M.; Jones, J. L.; Meng, Y. S. Correlation Between Oxygen Vacancy, Microstrain, and Cation Distribution in Lithium Excess Layered Oxides During the First Electrochemical Cycle. *Chem. Mater.* **2013**, *25* (9), 1621−1629.
(15) Cabana, J.; Kwon, B. J.; Hu, L. Mechanisms of Degradation and Strategies for the Stabilization of Cathode−Electrolyte Interfaces in Li Ion Batteries. *Acc. Chem. Res.* **2018**, *51* (2), 299−308.
(16) Xu, B.; Fell, C. R.; Chi, M.; Meng, Y. S. Identifying Surface Structural Changes in Layered Li Excess Nickel Manganese Oxides in High Voltage Lithium Ion Batteries: A Joint Experimental and Theoretical Study. *Energy Environ. Sci.* **2011**, *4* (6), 2223.
(17) Qian, D.; Xu, B.; Chi, M.; Meng, Y. S. Uncovering the Roles of Oxygen Vacancies in Cation Migration in Lithium Excess Layered Oxides. *Phys. Chem. Chem. Phys.* **2014**, *16* (28), 14665−14668.
(18) Lee, J.; Papp, J. K.; Clément, R. J.; Sallis, S.; Kwon, D. H.; Shi, T.; Yang, W.; McCloskey, B. D.; Ceder, G. Mitigating Oxygen Loss to Improve the Cycling Performance of High Capacity Cation Disordered Cathode Materials. *Nat. Commun.* **2017**, *8* (1), 981.
(19) Kim, H.; Byun, D.; Chang, W.; Jung, H. G.; Choi, W. A Nano $LiNbO_3$ Coating Layer and Diffusion Induced Surface Control towards High Performance 5 V Spinel Cathodes for Rechargeable Batteries. *J. Mater. Chem. A* **2017**, *5* (47), 25077−25089.
(20) Ohta, N.; Takada, K.; Sakaguchi, I.; Zhang, L.; Ma, R.; Fukuda, K.; Osada, M.; Sasaki, T. $LiNbO_3$ Coated $LiCoO_2$ as Cathode Material for All Solid State Lithium Secondary Batteries. *Electrochem. Commun.* **2007**, *9* (7), 1486−1490.
(21) Sebastian, L.; Gopalakrishnan, J. Li_2MTiO_4 (M = Mn, Fe, Co, Ni): New Cation Disordered Rocksalt Oxides Exhibiting Oxidative Deintercalation of Lithium. Synthesis of an Ordered Li_2NiTiO_4. *J. Solid State Chem.* **2003**, *172* (1), 171−177.
(22) Hoffmann, R.; Hoppe, R. Two New Variants of the Sodium Chloride Type of Structure: On Lithium Molybdenum Oxide (Li_4MoO_5) and Lithium Tungsten Oxide (Li_4WO_5). *Z. Anorg. Allg. Chem.* **1989**, *573*, 157−159.
(23) Yabuuchi, N.; Tahara, Y.; Komaba, S.; Kitada, S.; Kajiya, Y. Synthesis and Electrochemical Properties of Li_4MoO_5−NiO Binary System as Positive Electrode Materials for Rechargeable Lithium Batteries. *Chem. Mater.* **2016**, *28* (2), 416−419.
(24) Appapillai, A. T.; Mansour, A. N.; Cho, J.; Shao Horn, Y. Microstructure of $LiCoO_2$ with and without "$AlPO_4$" Nanoparticle Coating: Combined STEM and XPS Studies. *Chem. Mater.* **2007**, *19* (23), 5748−5757.
(25) Dahéron, L.; Dedryvère, R.; Martinez, H.; Flahaut, D.; Ménétrier, M.; Delmas, C.; Gonbeau, D. Possible Explanation for the Efficiency of Al Based Coatings on $LiCoO_2$: Surface Properties of $LiCo_{1-x}Al_xO_2$ Solid Solution. *Chem. Mater.* **2009**, *21* (23), 5607−5616.
(26) Glazier, S. L.; Li, J.; Zhou, J.; Bond, T.; Dahn, J. R. Characterization of Disordered $Li_{(1+x)}Ti_{2x}Fe_{(1-3x)}O_2$ as Positive Electrode Materials in Li Ion Batteries Using Percolation Theory. *Chem. Mater.* **2015**, *27* (22), 7751−7756.
(27) Twu, N.; Li, X.; Urban, A.; Balasubramanian, M.; Lee, J.; Liu, L.; Ceder, G. Designing New Lithium Excess Cathode Materials from Percolation Theory: Nanohighways in $Li_xNi_{2-4x/3}Sb_{x/3}O_2$. *Nano Lett.* **2015**, *15* (1), 596−602.
(28) Koga, H.; Croguennec, L.; Ménétrier, M.; Mannessiez, P.; Weill, F.; Delmas, C. Different Oxygen Redox Participation for Bulk and Surface: A Possible Global Explanation for the Cycling Mechanism of $Li_{1.20}Mn_{0.54}Co_{0.13}Ni_{0.13}O_2$. *J. Power Sources* **2013**, *236*, 250−258.
(29) Lee, J.; Seo, D. H.; Balasubramanian, M.; Twu, N.; Li, X.; Ceder, G. A New Class of High Capacity Cation Disordered Oxides for Rechargeable Lithium Batteries: Li−Ni−Ti−Mo Oxides. *Energy Environ. Sci.* **2015**, *8* (11), 3255−3265.
(30) Chen, Z.; Qin, Y.; Amine, K.; Sun, Y. K. Role of Surface Coating on Cathode Materials for Lithium Ion Batteries. *J. Mater. Chem.* **2010**, *20* (36), 7606.
(31) Schipper, F.; Bouzaglo, H.; Dixit, M.; Erickson, E. M.; Weigel, T.; Talianker, M.; Grinblat, J.; Burstein, L.; Schmidt, M.; Lampert, J.; et al. From Surface ZrO_2 Coating to Bulk Zr Doping by High Temperature Annealing of Nickel Rich Lithiated Oxides and Their Enhanced Electrochemical Performance in Lithium Ion Batteries. *Adv. Energy Mater.* **2018**, *8* (4), 1701682.
(32) Aurbach, D.; Levi, M. D.; Levi, E.; Teller, H.; Markovsky, B.; Salitra, G.; Heider, U.; Heider, L. Common Electroanalytical Behavior of Li Intercalation Processes into Graphite and Transition Metal Oxides. *J. Electrochem. Soc.* **1998**, *145* (9), 3024−3034.
(33) Amin, R.; Ravnsbæk, D. B.; Chiang, Y. M. Characterization of Electronic and Ionic Transport in $Li_{1-x}Ni_{0.8}Co_{0.15}Al_{0.05}O_2$ (NCA). *J. Electrochem. Soc.* **2015**, *162* (7), A1163−A1169.
(34) Twu, N.; Metzger, M.; Balasubramanian, M.; Marino, C.; Li, X.; Chen, H.; Gasteiger, H.; Ceder, G. Understanding the Origins of Higher Capacities at Faster Rates in Lithium Excess $Li_xNi_{2-4x/3}Sb_{x/3}O_2$. *Chem. Mater.* **2017**, *29* (6), 2584−2593.
(35) Strehle, B.; Kleiner, K.; Jung, R.; Chesneau, F.; Mendez, M.; Gasteiger, H. A.; Piana, M. The Role of Oxygen Release from Li and Mn Rich Layered Oxides During the First Cycles Investigated by On Line Electrochemical Mass Spectrometry. *J. Electrochem. Soc.* **2017**, *164* (2), A400−A406.
(36) Metzger, M.; Strehle, B.; Solchenbach, S.; Gasteiger, H. A. Origin of H_2 Evolution in LIBs: H_2O Reduction vs. Electrolyte Oxidation. *J. Electrochem. Soc.* **2016**, *163* (5), A798−A809.
(37) Berkes, B. B.; Schiele, A.; Sommer, H.; Brezesinski, T.; Janek, J. On the Gassing Behavior of Lithium Ion Batteries with NCM523 Cathodes. *J. Solid State Electrochem.* **2016**, *20* (11), 2961−2967.
(38) Renfrew, S. E.; McCloskey, B. D. Residual Lithium Carbonate Predominantly Accounts for First Cycle CO_2 and CO Outgassing of Li Stoichiometric and Li Rich Layered Transition Metal Oxides. *J. Am. Chem. Soc.* **2017**, *139* (49), 17853−17860.
(39) Hatsukade, T.; Schiele, A.; Hartmann, P.; Brezesinski, T.; Janek, J. Origin of Carbon Dioxide Evolved during Cycling of Nickel Rich Layered NCM Cathodes. *ACS Appl. Mater. Interfaces* **2018**, *10* (45), 38892−38899.
(40) Sathiya, M.; Rousse, G.; Ramesha, K.; Laisa, C. P.; Vezin, H.; Sougrati, M. T.; Doublet, M. L.; Foix, D.; Gonbeau, D.; Walker, W.; et al. Reversible Anionic Redox Chemistry in High Capacity Layered Oxide Electrodes. *Nat. Mater.* **2013**, *12* (9), 827−835.
(41) Tabuchi, M.; Nakashima, A.; Shigemura, H.; Ado, K.; Kobayashi, H.; Sakaebe, H.; Tatsumi, K.; Kageyama, H.; Nakamura, T.; Kanno, R. Fine $Li_{(4-x)/3}Ti_{(2-2x)/3}Fe_xO_2$ ($0.18 \leq x \leq 0.67$) Powder with Cubic Rock Salt Structure as a Positive Electrode Material for Rechargeable Lithium Batteries. *J. Mater. Chem.* **2003**, *13* (7), 1747−1757.
(42) Shigemura, H.; Tabuchi, M.; Sakaebe, H.; Kobayashi, H.; Kageyama, H. Lithium Extraction and Insertion Behavior of Nanocrystalline Li_2TiO_3 $LiFeO_2$ Solid Solution with Cubic Rock Salt Structure. *J. Electrochem. Soc.* **2003**, *150* (5), A638−A644.
(43) Yamamoto, T. Assignment of Pre Edge Peaks in K Edge x Ray Absorption Spectra of 3d Transition Metal Compounds: Electric Dipole or Quadrupole? *X Ray Spectrom.* **2008**, *37* (6), 572−584.
(44) Zhou, Y. N.; Ma, J.; Hu, E.; Yu, X.; Gu, L.; Nam, K. W.; Chen, L.; Wang, Z.; Yang, X. Q. Tuning Charge−Discharge Induced Unit Cell Breathing in Layer Structured Cathode Materials for Lithium Ion Batteries. *Nat. Commun.* **2014**, *5* (1), 5381.
(45) Thackeray, M. M.; Kang, S. H.; Johnson, C. S.; Vaughey, J. T.; Benedek, R.; Hackney, S. A. Li_2MnO_3 Stabilized $LiMO_2$ (M = Mn, Ni, Co) Electrodes for Lithium Ion Batteries. *J. Mater. Chem.* **2007**, *17* (30), 3112−3125.
(46) Lu, Z.; Dahn, J. R. Understanding the Anomalous Capacity of $Li/Li[Ni_xLi_{(1/3-2x/3)}Mn_{(2/3-x/3)}]O_2$ Cells Using In Situ X Ray Diffraction and Electrochemical Studies. *J. Electrochem. Soc.* **2002**, *149* (7), A815−A822.
(47) Deb, A.; Bergmann, U.; Cramer, S. P.; Cairns, E. J. Local Structure of $LiNi_{0.5}Mn_{0.5}O_2$ Cathode Material Probed by in Situ x Ray Absorption Spectroscopy. *J. Appl. Phys.* **2006**, *99* (6), 063701.

(48) Clément, R. J.; Kitchaev, D.; Lee, J.; Ceder, G. Short Range Order and Unusual Modes of Nickel Redox in a Fluorine Substituted Disordered Rocksalt Oxide Lithium Ion Cathode. *Chem. Mater.* **2018**, *30* (19), 6945−6956.
(49) Kitchaev, D. A.; Lun, Z.; Richards, W. D.; Ji, H.; Clément, R. J.; Balasubramanian, M.; Kwon, D. H.; Dai, K.; Papp, J. K.; Lei, T.; et al. Design Principles for High Transition Metal Capacity in Disordered Rocksalt Li Ion Cathodes. *Energy Environ. Sci.* **2018**, *11* (8), 2159−2171.
(50) Shin, Y.; Kan, W. H.; Aykol, M.; Papp, J. K.; McCloskey, B. D.; Chen, G.; Persson, K. A. Alleviating Oxygen Evolution from Li Excess Oxide Materials through Theory Guided Surface Protection. *Nat. Commun.* **2018**, *9* (1), 4597.
(51) Berkes, B. B.; Jozwiuk, A.; Vračar, M.; Sommer, H.; Brezesinski, T.; Janek, J. Online Continuous Flow Differential Electrochemical Mass Spectrometry with a Realistic Battery Setup for High Precision, Long Term Cycling Tests. *Anal. Chem.* **2015**, *87* (12), 5878−5883.
(52) Ravel, B.; Newville, M. ATHENA, ARTEMIS, HEPHAESTUS: Data Analysis for X Ray Absorption Spectroscopy Using IFEFFIT. *J. Synchrotron Radiat.* **2005**, *12* (4), 537−541.
(53) Ashiotis, G.; Deschildre, A.; Nawaz, Z.; Wright, J. P.; Karkoulis, D.; Picca, F. E.; Kieffer, J. The Fast Azimuthal Integration Python Library: PyFAI. *J. Appl. Crystallogr.* **2015**, *48* (2), 510−519.